Published in final edited form as:

Nat Photonics. 2016 May ; 10(5): 346–352. doi:10.1038/nphoton.2016.46.

Coherent coupling between radio frequency, optical, and acoustic waves in piezo-optomechanical circuits

Krishna C. Balram[1,2,*], **Marcelo I. Davanço**[1], **Jin Dong Song**[3], and **Kartik Srinivasan**[1,†]

[1]Center for Nanoscale Science and Technology, National Institute of Standards and Technology, Gaithersburg, MD 20899, USA

[2]Maryland NanoCenter, University of Maryland, College Park, MD 20742, USA

[3]Center for Opto-Electronic Materials and Devices Research, Korea Institute of Science and Technology, Seoul 136-791, South Korea

Abstract

Optomechanical cavities have been studied for applications ranging from sensing to quantum information science. Here, we develop a platform for nanoscale cavity optomechanical circuits in which optomechanical cavities supporting co-localized 1550 nm photons and 2.4 GHz phonons are combined with photonic and phononic waveguides. Working in GaAs facilitates manipulation of the localized mechanical mode either with a radio frequency (RF) field through the piezo-electric effect, which produces acoustic waves that are routed and coupled to the optomechanical cavity by phononic crystal waveguides, or optically through the strong photoelastic effect. Along with mechanical state preparation and sensitive readout, we use this to demonstrate an acoustic wave interference effect, similar to atomic coherent population trapping, in which RF-driven coherent mechanical motion is cancelled by optically-driven motion. Manipulating cavity optomechanical systems with equal facility through both photonic and phononic channels enables new architectures for signal transduction between the optical, electrical, and mechanical domains.

Introduction

The interaction of optical and mechanical degrees of freedom in chip-based nanoscale systems has been studied in many contexts, ranging from optomechanical cavities[1-4] in which localized optical and mechanical modes are coupled by radiation pressure, to waveguiding geometries in which propagating photons and phonons interact, as in stimulated Brillouin scattering[5-7] (the latter has also been studied in travelling-wave microresonators[8-10]). Recently there has been interest in combining the exquisite motion sensitivity of cavity optomechanical systems[11] with the radio frequency (RF) signal processing functionality of electromechanical systems to enable wavelength conversion

*Correspondence and requests for materials should be addressed to K.C.B. krishna.coimbatorebalram@nist.gov. †Correspondence and requests for materials should be addressed to K.S. kartik.srinivasan@nist.gov.

Author Contributions K.C.B. led the design, fabrication, and measurement of the devices, with assistance from M.D. and K.S. J.D.S. grew the epitaxial material, and K.C.B. and K.S. analyzed the data and wrote the manuscript, with input from all authors. K.S. supervised the project.

Competing financial interests The authors declare no competing financial interests.

between microwave and optical domains[12], electrostatically-actuated optomechanical cavities for sensing and feedback cooling[13,14], and piezo-optomechanical cavities[15,16] in which mechanical motion is driven by RF fields, with sensitive readout and coherent interference effects observable in the optical domain.

Here, we develop a platform in which a nanoscale optomechanical cavity is embedded in a larger system that enables access through both photonic and RF-driven phononic channels. Working in GaAs allows us to combine its photoelastic effect, which strongly couples localized optical and mechanical modes[17,18], with its piezoelectric behaviour, which enables the RF-driven generation of acoustic waves through an interdigitated transducer[19]. The generated acoustic waves are fed into phononic crystal waveguides that route and preferentially couple acoustic energy to the 2.4 GHz breathing mode of nanobeam optomechanical crystal cavities[18,20,21]. We use this combination of RF-driven acoustic waveguides and strong optomechanical coupling ($g_0/2\pi \approx 1.1$ MHz is more than one order of magnitude larger than that achieved in recent piezo-optomechanical cavities[15,16]) to demonstrate a number of effects. Phase-sensitive optical measurements confirm the ability to initialize the mechanical resonator with arbitrary amplitude and phase, and with an average coherent intracavity phonon population much less than one. We also observe a novel acoustic wave interference effect, similar to atomic coherent population trapping, in which RF-driven coherent motion of the mechanical resonator is cancelled by optically-induced motion, and vice versa. This demonstration of an optomechanical circuits platform which combines controlled excitation, routing, coupling, and detection of both propagating and localized photons and phonons will enable new applications of integrated electro-optomechanical systems in signal transduction and sensing.

Results

Figure 1(a) shows an overview of our platform[22]. The system uses an inter-digitated transducer (IDT) to convert an applied RF voltage to a propagating surface acoustic wave via the piezoelectric effect. This wave is routed using a phononic crystal waveguide and is butt-coupled to a nanobeam optomechanical crystal cavity (Fig. 1(c)-(d)). The optical interface to the cavity is via a fibre taper waveguide, which injects and extracts light from the device. Finally, a second IDT can electrically detect acoustic waves out-coupled from the cavity, or act as a second source of surface acoustic waves that couple to the cavity via a second phononic crystal waveguide.

Coupling Propagating and Localized Phononic Modes

Figure 1(b) shows the optomechanical crystal cavity design, which consists of an array of elliptical air holes in a suspended nanobeam[18]. The quadratic grade of the lattice constant and major and minor axis diameters of the elliptical holes co-localizes 1550 nm photons and 2.4 GHz phonons to a micrometre length scale. The optomechanical coupling rate $g_0/2\pi$, which is the optical cavity frequency shift due to zero-point motion, is ≈ 1.1 MHz and is dominated by the photoelastic effect. This is amongst the highest reported for an optomechanical cavity, and enables strong dynamic back-action so that the optical field can coherently manipulate the localized mechanical breathing mode. For RF-mediated coherent

control of the mechanical mode, we need to convert the RF voltage into an acoustic wave and route and couple the acoustic wave to the cavity. We begin by considering acoustic wave generation.

Surface acoustic waves (SAWs) have long been used in signal processing and communication[23,24]. Piezoelectric materials are used most extensively because of the ease of SAW excitation using IDTs, which are interleaved metal fingers biased with opposite polarity[22]. To take into account the multilayer metal electrode and underlying epitaxial layer structure (GaAs on $Al_{0.7}Ga_{0.3}As$), the IDT resonance frequency is determined from finite element method (FEM) simulations. Figure 2(a) shows the simulated SAW cross-section.

To route acoustic energy to the optomechanical cavity, we use phononic crystal waveguides. The phononic crystal design is adapted from the periodic cross-structure[25], which supports a complete bandgap[22]. The waveguide is a line defect geometry created by removing one row of crosses, resulting in a structure that supports laterally-confined, propagating acoustic modes. Figure 2(a) shows an FEM simulation of an acoustic wave excited by an IDT and propagating through the waveguide. The phononic crystal confines mechanical energy to the line defect region, with little displacement beyond a couple of periods transverse to the propagation direction.

We use FEM simulations to understand coupling between the localized and propagating mechanical modes. Figure 2(b) shows a simulation in which the waveguide mode at 2.25 GHz is launched into the nanobeam cavity, with excitation of the resonant mechanical breathing mode clearly observed. This coupling can be understood quantitatively from the cavity's acoustic reflection spectrum[22]. The finite intrinsic Q_m of the cavity in fabricated devices is modeled by a small imaginary component in the Young's modulus, with the magnitude adjusted for different Q_m. The reflection spectra (Fig. 2(b) inset) show the expected Lorentzian dip as the waveguide mode frequency sweeps over the cavity, with the depth determined by the coupling rate relative to the cavity intrinsic loss rate. For $Q_m = 1500$ (typical for our devices), the reflection contrast is limited to ≈ 15 %, while an improved intrinsic Q_m of 2.5×10^4 would enable critical coupling. Alternately, the transition between waveguide and cavity, or the waveguide geometry itself, can be tailored to modify the coupling rate. In contrast to recent work in which surface acoustic waves non-resonantly excited microring[26] and photonic crystal cavities[27], these simulations indicate that we can resonantly excite the localized mechanical mode of our nanobeam optomechanical crystal cavity. This is important for the experiments we describe going forward, given the large optomechanical coupling strength for this mode and its direct impact on high-sensitivity readout and manipulation of mechanical motion.

Experimentally, the IDT frequency response is measured by an electrical S_{11} (reflection) measurement. The top panel of Fig. 2(d) shows the S_{11} spectra for IDTs with electrode finger pitches of 1.05 μm and 1.1 μm. Optimal loading of the localized mechanical mode by the RF drive occurs when the mode frequency lies within the IDT bandwidth. The bottom panel of Fig. 2(d) shows the scaling of the IDT resonance frequency with finger pitch in simulation and experiment, along with the desired region of operation shaded in gray (corresponding to the nanobeam breathing mode frequency range). To ensure that some

fabricated devices show the required spectral overlap, each IDT addresses an array of optomechanical cavities (Fig. 1(a)), and the nanobeam width is varied across the array, thereby tuning the localized mechanical mode frequency with respect to a fixed IDT frequency[22].

While IDTs are a convenient means to generate propagating acoustic waves, the relatively small piezoelectric transduction coefficient of GaAs[23] limits the conversion efficiency back to the RF domain for electrical readout. Thus, for sensitive detection of the nanobeam cavity's motion when driven by the propagating acoustic wave, we use the strong photoelastic coupling for optical readout. The setup is shown in Fig. 2(c), where light is injected into the optomechanical cavity using an optical fibre taper waveguide, and a vector network analyzer (VNA) drives the IDT with an RF voltage and coherently detects the photocurrent signal transmitted past the optomechanical cavity, yielding a piezo-optic S_{21} measurement. The laser wavelength is positioned on the shoulder of the optical mode (Q_{opt} = 36600±400, fit uncertainty 95 % confidence intervals)[22], so that the phase fluctuations induced by motion are transduced into an intensity-modulated optical signal.

The bottom panel of Fig. 2(e) shows the measured piezo-optic S_{21} in two instances. First (red curve), a phononic crystal waveguide butt-coupled to the optomechanical cavity is adjacent to the RF-driven IDT (IDT 1, Fig. 2(c)), and a pronounced peak ≈ 20 dB above the background is observed at the nanobeam cavity's mechanical mode frequency, as confirmed by direct detection of its thermal noise spectrum (top panel of Fig. 2(e)). In the second case (blue curve), an unperturbed phononic shield spans the region between the cavity and RF-driven IDT (IDT 2, Fig. 2(c)). Here, the piezo-optic S_{21} is suppressed by more than 30 dB relative to the first case, indicating that the phononic shield effectively blocks the transmission of acoustic energy from the IDT to the cavity.

Coherent Mechanical State Preparation and Readout

Next, we phase coherently load mechanical states into our optomechanical cavity via the phononic waveguide, and show that the optical readout is sensitive enough to distinguish a fraction of a coherent phonon from the thermal phonon population ($N_{avg} \approx 2600$) and measurement noise. Figure 3(a) shows the setup (see Methods), where in comparison to Fig. 2(c), we now additionally provide RF phase control, calibration of the optomechanical coupling rate, and measurement of the total RF power spectral density (PSD), consisting of the incoherent thermal motion of the mechanical resonator, its driven coherent motion due to surface acoustic wave excitation, and the phase modulator calibration tone.

Figure 3(b) displays the piezo-optic S_{21} measurement of coherently-driven motion similar to Fig. 2(e), but now for an optomechanical cavity connected to input/output phononic waveguides (Fig. 3(a)). The results are similar, with the piezo-optic S_{21} showing a peak corresponding to the cavity's mechanical resonance frequency and which lies within the IDT's resonance bandwidth. The importance of this overlap is shown in Fig. 3(e)-(f), which contrasts the RF power applied to the IDT to achieve a certain coherent intracavity phonon population when the localized nanobeam mechanical mode is on-resonance with the IDT (Fig. 3(c)) to when it is off-resonance with the IDT (Fig. 3(d)). Two nanobeam cavities from

the same array were chosen, so that the IDT characteristics were fixed as the nanobeam mechanical frequency changed. Off resonance, nearly 20 dB greater RF input power is needed to achieve the same strength of the coherent tone in the photodetected signal, reflecting the resonant nature of the IDT.

We quantify the average coherent intracavity phonon number N_{ph}^{coh} by comparing the strength of the coherent tone with that due to the integrated thermally-driven motion $S_{\mathrm{th}}(\Omega_m)$. That is:

$$N_{ph}^{coh}=\frac{k_B T}{\hbar\Omega_m}\frac{S_{coh}\left(\Omega_{coh}\right)}{S_{th}\left(\Omega_m\right)} \quad (1)$$

where k_{B} is Boltzmann's constant, T is temperature (298 K ± 5 K), Ω_m is the mechanical mode frequency, $S_{\mathrm{coh}}(\Omega_{\mathrm{coh}})$ is the power in the coherent tone, and $S_{\mathrm{th}}(\Omega_m)$ is the integrated power in the thermal noise peak. $N_{ph}^{coh}=43\pm1.5$ for Fig. 3(e) and $N_{ph}^{coh}=50\pm1.8$ for Fig. 3(f), quantifying the increased RF drive needed to achieve a given N_{ph}^{coh} when the nanobeam mechanical resonance and IDT are spectrally misaligned. Finally, we use the phase modulator to measure $g_0/2\pi$ = 1.1 MHz ± 60 kHz, corresponding well with simulations[18], and with a one standard deviation uncertainty set by the uncertainty in the phase modulator V_π[22].

We can also consider the device in Fig. 3(c) as a resonant acousto-optic phase modulator (an exact comparison in the sideband-resolved regime), and determine its half-wave voltage $V_\pi \approx 652$ mV[22]. This can be reduced to $V_\pi < 100$ mV by optimizing the coupling to the optomechanical cavity and minimizing both RF and acoustic reflections and scattering at interfaces. Recently, Li and colleagues have demonstrated up to 12 GHz on-chip acousto-optic modulators in which surface acoustic waves modulate the response of a photonic crystal cavity[27]. In contrast to this work and earlier papers[19,26], here the propagating acoustic waves are laterally confined and resonantly couple to localized mechanical modes. The localized mechanical resonance enhances the modulation efficiency (by ~ $\sqrt{Q_m}$) without creating a significant bandwidth restriction beyond that already imposed by the IDT[22]. Moreover, such localized mechanical modes are typically more strongly coupled to localized optical modes.

For coherent control of the resonator, we need to transfer both the RF amplitude and phase onto the cavity displacement. Figure 3(g) plots the in-phase and quadrature components of the photodetected signal on-resonance for different phases applied to the IDT. Th e data is displayed as a function of average coherent mechanical displacement, where the calibration described in the previous paragraph is used to determine N_{ph}^{coh}, which in turn is converted to a displacement by:

$$N_{ph}^{coh}=\frac{1}{2}\left(\frac{\alpha_{cav}}{x_{zpf}}\right)^2 \quad (2)$$

where α_{cav} is the magnitude of the coherent cavity displacement and $x_{zpf}=\sqrt{\frac{\hbar}{2m_{eff}\Omega_m}}$ is the zero-point motional amplitude ($m_{eff} \approx 0.5$ pg is the simulated effective mass). The data shows that a variation in amplitude and phase of the RF signal is mapped onto the localized mechanical mode, and it can be initialized at an arbitrary location in phase space. These measurements confirm that coherence is preserved through the process of converting an RF voltage to an acoustic wave that propagates through a phononic crystal waveguide and couples to an optomechanical crystal cavity. By injecting acoustic waves with similar amplitudes and varying phase difference through two phononic waveguides that excite the same optomechanical cavity, we can observe constructive and destructive interference effects occurring within the mechanical resonator[22].

The combination of coherent detection and the large optomechanical coupling strength enables measurement of a weak coherent intracavity phonon population on top of the ≈ 2600 thermal phonons in the cavity. In Fig. 3(h), we reduce the RF amplitude and measure the mechanical motion on-resonance, displayed as a polar plot in terms of the phonon number and phase angle. Figure 3(i) shows the data plotted against motional amplitude for the three smallest RF drives, where for each the data has been histogrammed into 15 equally-spaced bins. $N_{ph}^{coh} \approx 1.1$ is well-separated from the measurement noise floor (RF set to zero), and N_{ph}^{coh} as low as ≈ 0.05 is resolvable. We also display the PSD for $N_{ph}^{coh}<1$ (Fig. 3(h) inset). The minimum detectable $N_{ph}^{coh} \approx 0.05$ is approximately 20× smaller than in Ref. 15, and is primarily due to the significantly larger optomechanical coupling rate of 1.1 MHz (compared to 30 kHz in Ref. 15).

Coherent Interactions between RF, Optics, and Mechanics

Thus far, we have shown that phononic crystal waveguides sourced by IDTs can effectively couple acoustic energy to the localized mechanical mode of a nanobeam optomechanical cavity. In these experiments, large g_0 enables sensitive optical readout of the mechanical motion, but was not used to manipulate the mechanical resonator. We next consider experiments in which the mechanical resonator is simultaneously excited using both RF signals and optical fields. This highlights a key feature of the GaAs optomechanical circuit platform, which is that the motion of the mechanical resonator can be manipulated with similar facility along either the optical or RF channel.

Figure 4(a) shows a schematic indicating the couplings and decay channels of the different components in our system. If we ignore the states that depict the phononic waveguide, its feeding from an IDT, and coupling to the phononic cavity, we recover the characteristic Λ-system configuration in which optomechanically induced transparency (OMIT)[28-30] has been observed in many systems. Adding the new channel provides us with another knob to

coherently control and probe the system properties and observe new phenomena. The interference effect we describe in this section occurs in the phononic cavity, which can be driven optically via the beating of probe and control lasers that are detuned from each other by the mechanical mode frequency (as in OMIT), or acoustically through the phononic waveguide. These two pathways can be tuned to have equal amplitudes and opposite phases, resulting in a cancellation of the coherent motion of the mechanical resonator. This effect is qualitatively similar to coherent population trapping in atomic systems[31,32], and has not been previously discussed or observed in recent studies of piezo-optomechanical systems[15,16,26,27].

Starting with the coupled equations of cavity optomechanics, one can derive an expression for the steady-state cavity displacement amplitude β_{d+}[22]:

$$\beta_{d+}=\frac{-ig_0\left(\alpha_0\alpha^*_{d-}\right)-\sqrt{\frac{\gamma_e}{2}}\beta_{\mathrm{in},0}e^{i\Psi}}{i\left(\Omega_m-\Omega_d\right)+\frac{\gamma_i}{2}} \quad (3)$$

The first term in the numerator corresponds to the optical drive due to beating of the intracavity control (α_0) and probe (α_{d-}) beams, and the second term corresponds to the acoustic drive ($\beta_{in,0}e^{i\Psi}$) through the phononic waveguide coupling to the cavity (coupling rate γ_e and intrinsic decay rate γ_i). Appropriate choice of the amplitude ($\beta_{in,0}$) and phase (Ψ) of the acoustic drive produces the condition for cancellation of the mechanical mode (β_{d+} = 0):

$$\sqrt{\frac{\gamma_e}{2}}\beta_{\mathrm{in},0}e^{i\Psi}=\frac{-i\sqrt{\frac{\kappa_e}{2}}g_0\alpha_0\alpha^*_{in,-}}{-i\left(\Delta+\Omega_d\right)+\frac{\kappa_i}{2}} \quad (4)$$

wherein $\alpha_{in,-}$ represents the input probe signal, Δ the laser-cavity detuning, Ω_d the probe beam detuning from the control beam frequency, κ_e the optical cavity coupling rate, and κ_i the intrinsic optical cavity decay rate.

When this condition is satisfied, the coherent cavity displacement tends to zero and the cavity transmission is flat over the mechanical resonator bandwidth (the system acts as a pure optical cavity for the probe). Only the coherently driven component of the cavity displacement becomes zero, as the cavity is still driven by incoherent thermal motion and has a finite PSD. We also distinguish this effect from other phenomena observed in cavity optomechanics. Both OMIT and electromechanically-induced optical transparency[15,16] are effects in which probe photons optically interfere with light scattered off a driven mechanical resonator, and the mechanical resonator has a finite coherent displacement amplitude at all times. The effect we observe is similar to the optomechanical dark mode[33,34] established in coherent wavelength conversion[34-36], although in that work coherent mechanical motion is suppressed purely though optomechanical coupling.

Figure 4(b) shows the experimental setup used to probe the coherent interaction between RF, optics, and mechanics, where the RF signals driving the IDT and electro-optic phase

modulator are coherent but can differ in amplitude and overall phase (see Methods). Figure 4(c) shows a series of piezo-optical S_{21} measurements performed as the VNA output frequency is swept across the mechanical resonance and the RF power into the IDT is increased, along with calculations of the expected S_{21} spectrum and corresponding mechanical resonator displacement amplitude[22]. The topmost black curves are for the IDT channel turned off, and correspond to the pure OMIT case. We then increase the RF power while keeping the phase fixed to satisfy the condition for acoustic wave interference. As the RF power is increased, the OMIT peak is reduced and at a particular RF power (cyan curves in Fig. 4(d)), the transmission spectrum reaches zero on-resonance and is approximately (perfectly) spectrally flat in experiment (theory). This corresponds to complete suppression of the coherent cavity displacement and removal of the transparency window that was initially induced by the optomechanical interaction. The inability to achieve perfect spectral flatness in experiment is attributed to the actuation of other mechanical modes that occurs electrically but not optically[22]. With further increase in the RF power, the cavity is primarily driven by the phononic waveguide and the cavity displacement amplitude increases correspondingly (magenta, yellow, dark gray curves). Since the phase is set for destructive interference, the probe transmission drops and the interference feature within the optical cavity spectrum re-appears (the system is now in the regime of electromechanically-induced optical transparency[15,16]). Here, the mechanical breathing mode is in the same state as in pure OMIT, except that the displacement has the opposite phase and so transparency is converted to absorption.

A more complete picture is observed by measuring the in-phase and quadrature components of the on-resonance photodetected signal (Fig. 4(d)). Starting with the pure OMIT condition (IDT turned off, Fig. 4(e), curve i), as we increase the RF drive to the IDT, for the right choice of phase the cavity displacement approaches zero (Fig. 4(e), curve ii), and the signal on-resonance is equal to its off-resonance value (Fig. 4(e), dashed circle). Further increase in the RF power moves the system into the region of induced absorption (Fig. 4(e), curve iii), while other parts of phase space are accessed by varying the phase applied to the IDT. For an arbitrary phase, the response of the system is given by an asymmetric Fano lineshape (for example, Fig. 4(e), curve iv).

Discussion

We have presented an integrated piezo-optomechanical circuit platform in which fibre-coupled GaAs optomechanical crystal cavities are interfaced with phononic waveguides and interdigitated transducers. This system combines localized and interacting 1550 nm photons and 2.4 GHz phonons with excitation and readout along either the optical or mechanical channel, with the latter connected to the RF domain via IDTs. As GaAs is both piezoelectric and has a strong photoelastic effect, the mechanical resonator can be effectively manipulated by both RF and optical fields, enabling potential applications such as RF-controllable optomechanically-induced transparency for slow light and delay lines[30] and phononic routing between cavity optomechanical nodes for quantum networks[37,38]. Generation of acoustic waves with optimized IDTs[23,39] or through optical means via stimulated Brillouin scattering[5-7] and developments in chip-based phononics[40,41,41-44] can improve future circuitry to interface with the optomechanical cavities. Finally, incorporation of InAs/GaAs

quantum dots[45-47], which have been used in many quantum optics applications[48] and are compatible with the device fabrication described here, would add qualitatively new functionality.

Methods

Measurement methods

Light from a 1520 nm to 1630 nm tunable laser is coupled into and out of the optomechanical cavities using an optical fibre taper waveguide with a minimum diameter of $\approx 1\ \mu$m, with the output optical signal photodetected by an avalanche photodiode (APD). For coherent excitation and detection of mechanical motion (piezo-optic S_{21}) as in Fig. 2(c), a vector network analyzer (VNA) excites a source IDT and reads out the coherent component of the photodetected signal. To initialize the mechanical resonator at an arbitrary location in phase space, an RF phase shifter is placed between the VNA output and source IDT (Fig. 3(a)). For simultaneous excitation of the mechanical resonator by both RF and optical fields, the output of the VNA is split into two paths, with one path driving an electro-optic phase modulator inserted at the output of the tunable laser, and the other path sent through an RF amplifier and phase shifter before going to the source IDT (Fig. 4(b)). This enables control of the amplitude and phase of the RF signal driving the IDT with respect to that driving the phase modulator. In these experiments (Fig. 4), the control laser power is fixed and is blue-detuned by a mechanical resonance frequency from the optical cavity resonance.

Measurement of the total photodetected signal (not just the coherent component) is obtained by sending it to a real-time RF spectrum analyzer (RSA) (Fig. 3(a)); this is used to calibrate the coherent intracavity phonon number with respect to thermal noise. Finally, a second RF signal generator is used for calibration of the optomechanical coupling rate g_0 (Fig. 3(a)), as discussed in detail in the supplementary material[22].

Fabrication

A detailed description of the fabrication procedure is provided in the supplementary material[22], and a brief summary is provided here. The IDTs are defined first through electron-beam lithography and metal lift-off. After electrical S_{11} measurements to determine the IDT resonance frequencies, the phononic crystal waveguides and nanobeam optomechanical crystal patterns are overlaid with a second electron-beam lithography step that uses alignment marks defined during the IDT fabrication. The patterns are then transferred to the GaAs layer using an Ar/Cl_2 inductively-coupled plasma reactive ion etch step. The devices are finally released using a timed wet etch.

Simulations

A detailed description of all the simulation procedures is provided in the supplementary material[22], and a brief summary is provided here. First, we use a finite element method (FEM) solver to calculate both the resonance frequency of the nanobeam cavity's localized mechanical mode and the surface acoustic wave generated by the IDT for a given pitch. In a separate simulation, this IDT-generated surface acoustic wave is launched into the phononic crystal line defect waveguide, and penetration of mechanical energy into the surrounding

phononic shield was examined as a function of acoustic wave frequency. The coupling between the phononic crystal waveguide and nanobeam optomechanical cavity was calculated by defining an acoustic Poynting vector and solving for the transmitted and reflected acoustic power as a function of frequency. For the acoustic wave interference simulations, the coupled equations for intracavity optical field amplitude and mechanical displacement were solved numerically by linearizing around the steady-state values. Finally, the nanobeam optomechanical cavity's optical modes were solved using an FEM solver, and the optomechanical coupling rate to the localized mechanical breathing mode was determined from a calculation based on perturbation theory, taking into account the effect of both moving dielectric boundaries and the photoelastic effect.

Supplementary Material

Refer to Web version on PubMed Central for supplementary material.

Acknowledgements

K.C.B. acknowledges support under the Cooperative Research Agreement between the University of Maryland and NIST-CNST, Award 70NANB10H193. J.D.S acknowledges the support from the KIST flag-ship institutional program. The authors thank D. Rutter and A. Band for help with microwave electronics. This work was partially supported by the DARPA MESO program.

References

1. Aspelmeyer M, Kippenberg TJ, Marquardt F. Cavity optomechanics. Rev. Mod. Phys. 2014; 86:1391.
2. Metcalfe M. Applications of cavity optomechanics. Applied Physics Reviews. 2014; 1:031105.
3. Favero I, Karrai K. Optomechanics of deformable optical cavities. Nature Photon. 2009; 3:201–205.
4. Kippenberg TJ, Vahala KJ. Cavity Optomechanics: Back-Action at the Mesoscale. Science. 2008; 321:1172–1176. [PubMed: 18755966]
5. Pant R, et al. On-chip stimulated brillouin scattering. Opt. Express. 2011; 19:8285–8290. [PubMed: 21643078]
6. Shin H, et al. Tailorable stimulated Brillouin scattering in nanoscale silicon waveguides. Nature Commun. 2013; 4
7. Van Laer R, Kuyken B, Van Thourhout D, Baets R. Interaction between light and highly confined hypersound in a silicon photonic nanowire. Nature Photon. 2015; 9:199–203.
8. Matsko A, Savchenkov A, Ilchenko V, Seidel D, Maleki L. Optomechanics with surface-acoustic-wave1 whispering-gallery modes. Phys. Rev. Lett. 2009; 103:257403. [PubMed: 20366282]
9. Bahl G, Zehnpfennig J, Tomes M, Carmon T. Stimulated optomechanical excitation of surface acoustic waves in a microdevice. Nature Commun. 2011; 2:403. [PubMed: 21792182]
10. Li J, Lee H, Vahala KJ. Microwave synthesizer using an on-chip brillouin oscillator. Nature Commun. 2013; 4
11. Wilson DJ, et al. Measurement-based control of a mechanical oscillator at its thermal decoherence rate. Nature (London). 2015; 524:325–329. [PubMed: 26258303]
12. Andrews R, et al. Bidirectional and efficient conversion between microwave and optical light. Nature Phys. 2014; 10:321–326.
13. Winger M, et al. A chip-scale integrated cavity-electro-optomechanics platform. Opt. Express. 2011; 19:24905–24921. [PubMed: 22273884]
14. Miao H, Srinivasan K, Aksyuk V. A microelectromechanically controlled cavity optomechanical sensing system. New J. Phys. 2012; 14:075015.

15. Bochmann J, Vainsencher A, Awschalom DD, Cleland AN. Nanomechanical coupling between microwave and optical photons. Nature Phys. 2013; 9:712–716.
16. Fong KY, Fan L, Jiang L, Han X, Tang HX. Microwave-assisted coherent and nonlinear control in cavity piezo-optomechanical systems. Phys. Rev. A. 2014; 90:051801.
17. Baker C, et al. Photoelastic coupling in gallium arsenide optomechanical disk resonators. Opt. Express. 2014; 22:14072–14086. [PubMed: 24977505]
18. Balram KC, Davanço M, Lim JY, Song JD, Srinivasan K. Moving boundary and photoelastic coupling in gaas optomechanical resonators. Optica. 2014; 1:414–420.
19. Mauricio M, de Lima J, Santos PV. Modulation of photonic structures by surface acoustic waves. Rep. Prog. Phys. 2005; 68:1639.
20. Eichenfield M, Chan J, Camacho RM, Vahala KJ, Painter O. Optomechanical crystals. Nature. 2009; 462:78–82. [PubMed: 19838165]
21. Chan J, Safavi-Naeini AH, Hill JT, Meenehan S, Painter O. Optimized optomechanical crystal cavity with acoustic radiation shield. Appl. Phys. Lett. 2012; 101:081115.
22. See Supplementary Material for additional information on device fabrication, simulations of the interdigitated transducers and phononic crystal waveguides, and measurements of acoustic wave interference effects.
23. Campbell CK. Applications of surface acoustic and shallow bulk acoustic wave devices. Proc. IEEE. 1989; 77:1453–1484.
24. Campbell, C. Surface acoustic wave devices for mobile and wireless communications. Academic press; 1998.
25. Safavi-Naeini AH, Painter O. Design of optomechanical cavities and waveguides on a simultaneous bandgap phononic-photonic crystal slab. Opt. Express. 2010; 18:14926–14943. [PubMed: 20639979]
26. Tadesse SA, Li M. Sub-optical wavelength acoustic wave modulation of integrated photonic resonators at microwave frequencies. Nature Commun. 2014; 5
27. Li H, Tadesse SA, Liu Q, Li M. Nanophotonic cavity optomechanics with propagating acoustic waves at frequencies up to 12 ghz. Optica. 2015; 2:826–831.
28. Agarwal G, Huang S. Electromagnetically induced transparency in mechanical effects of light. Phys. Rev. A. 2010; 81:041803.
29. Weis S, et al. Optomechanically Induced Transparency. Science. 2010; 330:1520–1523. [PubMed: 21071628]
30. Safavi-Naeini AH, et al. Electromagnetically induced transparency and slow light with optomechanics. Nature (London). 2011; 472:69–73. [PubMed: 21412237]
31. Arimondo, E. Coherent Populating Trapping in Laser Spectroscopy. Elsevier Science; 1996. p. 257-354.
32. Khan, S.; Kumar, M.; Chanu, SR.; Bharti, V.; Natarajan, V. Coherent population trapping (CPT) versus Electromagnetically induced transparency (EIT). 2015. arXiv:1503.06956
33. Wang Y-D, Clerk AA. Using interference for high fidelity quantum state transfer in optomechanics. Phys. Rev. Lett. 2012; 108:153603. [PubMed: 22587252]
34. Dong C, Fiore V, Kuzyk MC, Wang H. Optomechanical dark mode. Science. 2012; 338:1609–1613. [PubMed: 23160956]
35. Hill JT, Safavi-Naeini AH, Chan J, Painter O. Coherent optical wavelength conversion via cavityoptomechanics. Nature Commun. 2012; 3:1196. [PubMed: 23149741]
36. Liu Y, Davanço M, Aksyuk V, Srinivasan K. Electromagnetically induced transparency and wideband wavelength conversion in silicon nitride microdisk optomechanical resonators. Phys. Rev. Lett. 2013; 110:223603. [PubMed: 23767723]
37. Safavi-Naeini AH, Painter O. Proposal for an optomechanical traveling wave phonon-photon translator. New J. Phys. 2011; 13:013017.
38. Habraken S, Stannigel K, Lukin MD, Zoller P, Rabl P. Continuous mode cooling and phonon routers for phononic quantum networks. New J. Phys. 2012; 14:115004.
39. de Lima M Jr, Alsina F, Seidel W, Santos P. Focusing of surface-acoustic-wave fields on (100) gaas surfaces. J. Appl. Phys. 2003; 94:7848–7855.

40. Khelif A, Choujaa A, Benchabane S, Djafari-Rouhani B, Laude V. Guiding and bending of acoustic waves in highly confined phononic crystal waveguides. Appl. Phys. Lett. 2004; 84:4400–4402.
41. Maldovan M. Sound and heat revolutions in phononics. Nature. 2013; 503:209–217. [PubMed: 24226887]
42. Olsson Iii R, El-Kady I. Microfabricated phononic crystal devices and applications. Measurement Science and Technology. 2009; 20:012002.
43. Hatanaka D, Mahboob I, Onomitsu K, Yamaguchi H. Phonon waveguides for electromechanical circuits. Nature Nanotech. 2014; 9:520–524.
44. Mohammadi S, Adibi A. On chip complex signal processing devices using coupled phononic crystal slab resonators and waveguides. AIP Advances. 2011; 1:041903.
45. Metcalfe M, Carr SM, Muller A, Solomon GS, Lawall J. Resolved Sideband Emission of InAs/GaAs Quantum Dots Strained by Surface Acoustic Waves. Phys. Rev. Lett. 2010; 105:037401. [PubMed: 20867805]
46. Fuhrmann DA, et al. Dynamic modulation of photonic crystal nanocavities using gigahertz acoustic phonons. Nature Photon. 2011; 5:605–609.
47. Yeo I, et al. Strain-mediated coupling in a quantum dot-mechanical oscillator hybrid system. Nature Nanotech. 2013
48. Lodahl P, Mahmoodian S, Stobbe S. Interfacing single photons and single quantum dots with photonic nanostructures. Rev. Mod. Phys. 2015; 87:347.

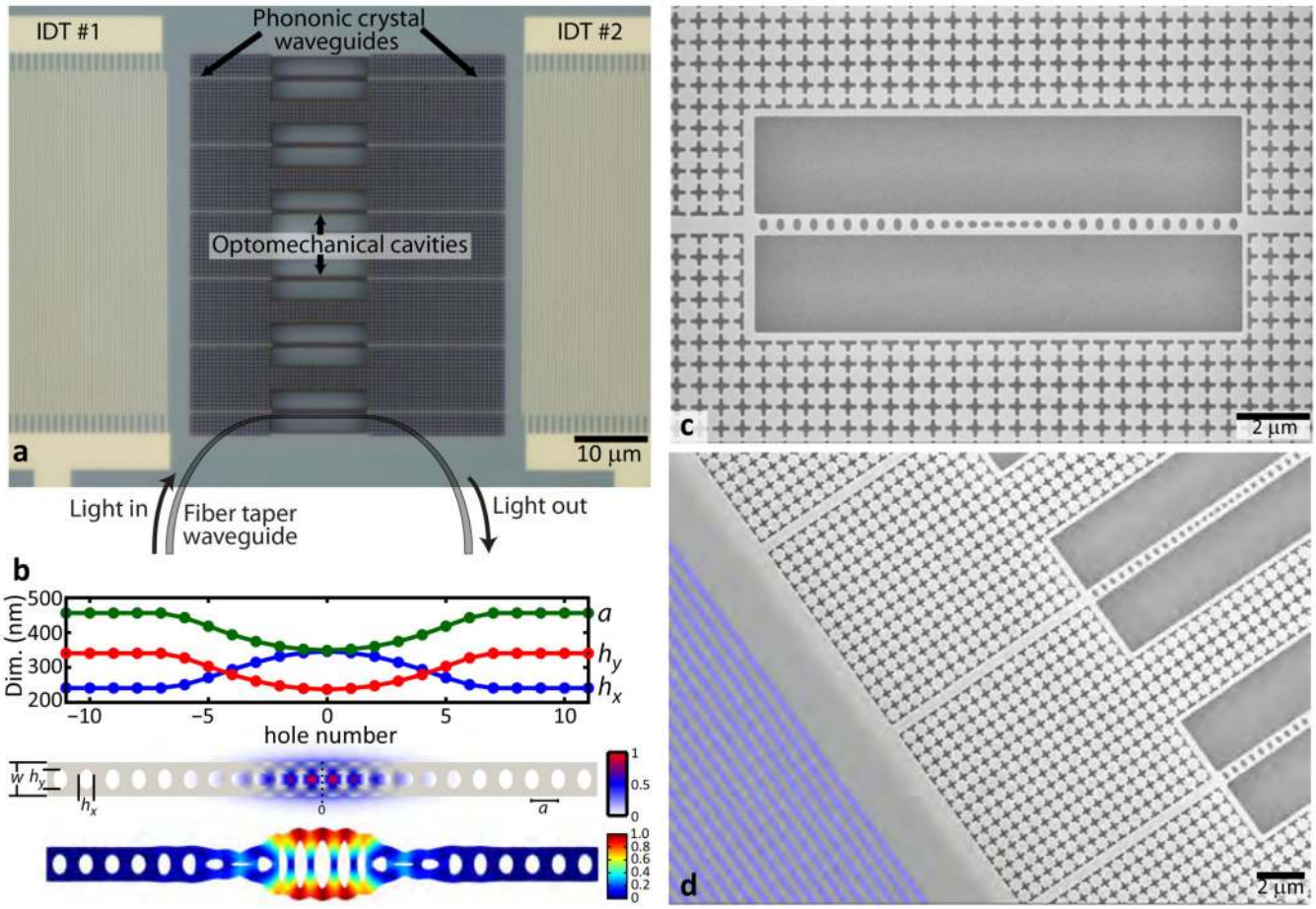

FIG. 1. Piezo-optomechanical circuits

(a) Optical micrograph of the device layout. An array of optomechanical cavities, each coupled to input and output phononic crystal waveguides, is placed between inter-digitated transducers (IDTs) that excite and/or detect surface acoustic waves. Optical coupling is done using a fibre taper waveguide, shown schematically in gray. (b) Optomechanical crystal cavity design. (Top) Variation of the lattice constant, major axis diameter, and minor axis diameter of the elliptical holes along the nanobeam; (Middle) Simulated normalized electric field amplitude for the 1550 nm optical mode. (Bottom) Simulated normalized displacement amplitude for the 2.4 GHz mechanical breathing mode. (c) Scanning electron microscope (SEM) image of a nanobeam optomechanical crystal cavity, including the adjacent input and output phononic crystal waveguides. (d) SEM image showing the transition from the input IDT (shaded in blue) to the phononic crystal waveguide and nanobeam cavity.

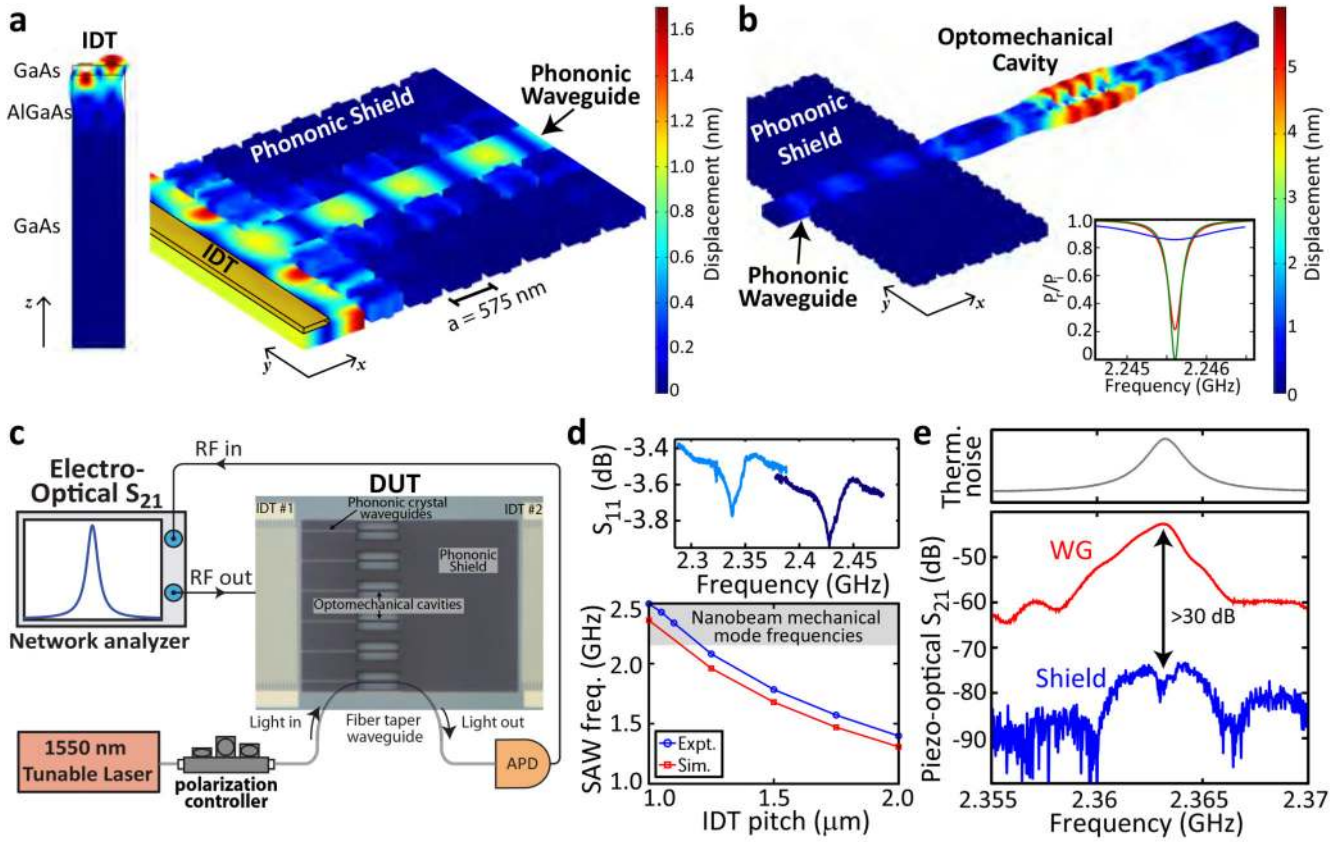

FIG. 2. Coupling between propagating and localized phononic modes

FEM simulation of (a) surface acoustic wave (SAW) generation by an IDT (left) and its propagation in a phononic crystal waveguide (right) and (b) coupling between the phononic crytsal waveguide and nanobeam cavity modes. The inset plots the acoustic reflection spectrum, for Q_m of 1.5×10^3 (blue), 1.5×10^4 (red), and 2.5×10^4 (green). (c) Setup for optical readout of the nanobeam's coherent mechanical motion, driven either through a phononic crystal waveguide (IDT 1) or a phononic shield (IDT 2). (d) (Top) IDT reflection spectrum (S_{11}) for two different finger spacings. (Bottom) Experimental (blue) and theoretical (red) IDT resonance frequency vs. IDT pitch. (e) (Top) Thermal noise spectrum of the nanobeam cavity's localized mechanical mode. The y-axis span is 10 dB. (Bottom) Coherently-detected nanobeam mechanical motion spectrum (piezo-optic S_{21}), when driven through a phononic crystal waveguide (red) and through the phononic shield (blue).

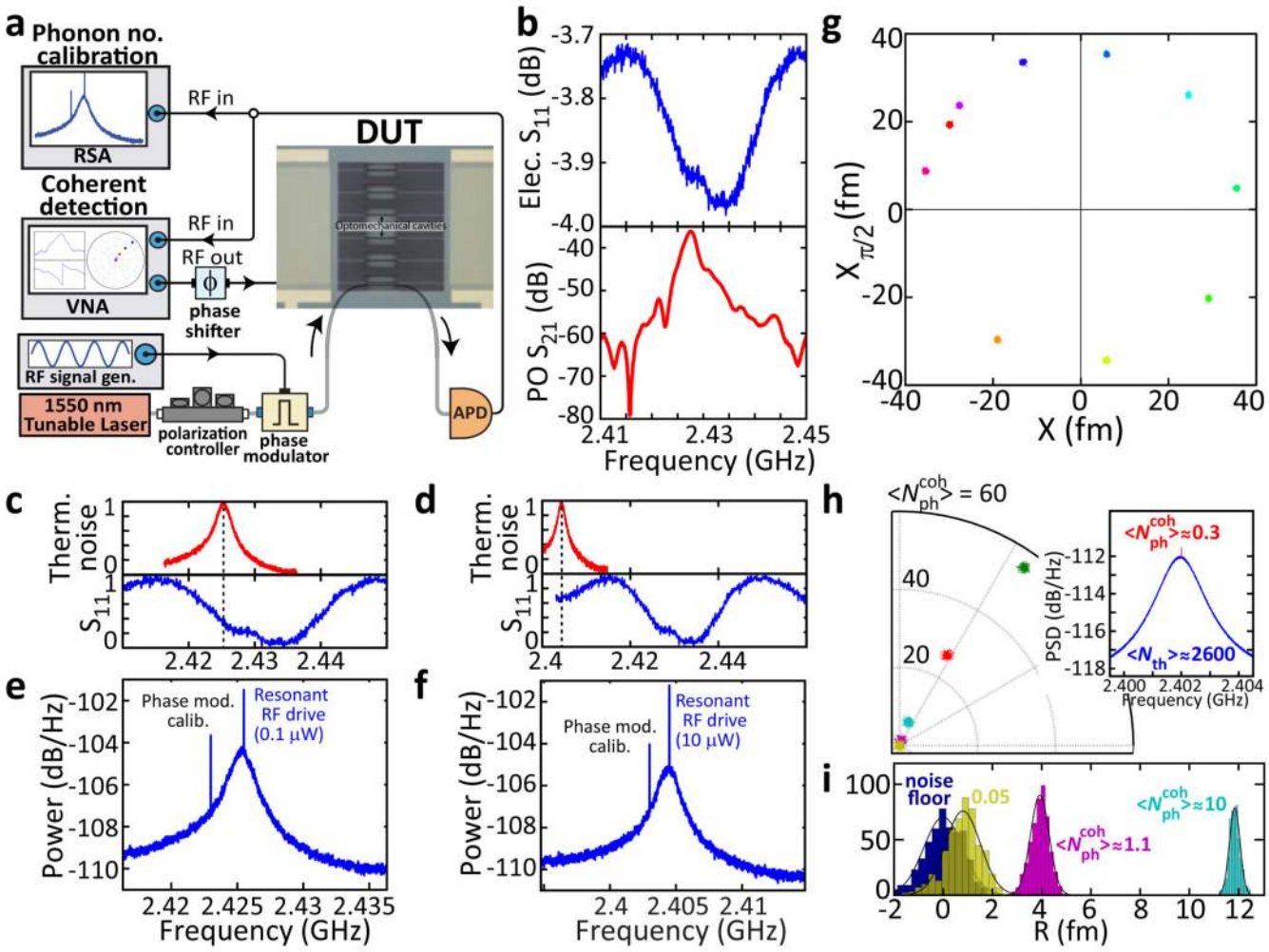

FIG. 3. Acousto-optic modulation and coherent phonon detection

(a) Setup for determining the average coherent intracavity phonon number $\mathcal{N}^{\mathrm{coh}}_{\mathrm{ph}}$ through comparison with thermal motion. (b) IDT S_{11}(top) and piezo-optic S_{21} (bottom) for a spectrally aligned IDT and nanobeam. (c)-(d) Thermal noise spectrum of the localized mechanical mode (red, RF off) and IDT S_{11} (blue) when they are spectrally (c) aligned and (d) misaligned. (e)-(f) Corresponding total photodetected spectrum (PSD) with the RF drive on, with $\mathcal{N}^{\mathrm{coh}}_{\mathrm{ph}} = 43 \pm 1.5$ in (e) and $\mathcal{N}^{\mathrm{coh}}_{\mathrm{ph}} = 50 \pm 1.8$ in (f). The RF power is increased by 20 dB in (f). (g) Quadrature plot with $\mathcal{N}^{\mathrm{coh}}_{\mathrm{ph}} = 91 \pm 3.3$ and varying phase (measurement bandwidth = 200 Hz). (h) (Left) Polar plot of $\mathcal{N}^{\mathrm{coh}}_{\mathrm{ph}}$ with decreasing RF drive. (Right) Total PSD for $\mathcal{N}^{\mathrm{coh}}_{\mathrm{ph}} = 0.3 \pm 0.01$. (i) Histogram data from (h) for small motional amplitudes (bandwidth = 20 Hz). Phonon number uncertainty (1σ) is from the combined uncertainty in sample temperature, PSD fit, and RSA error.

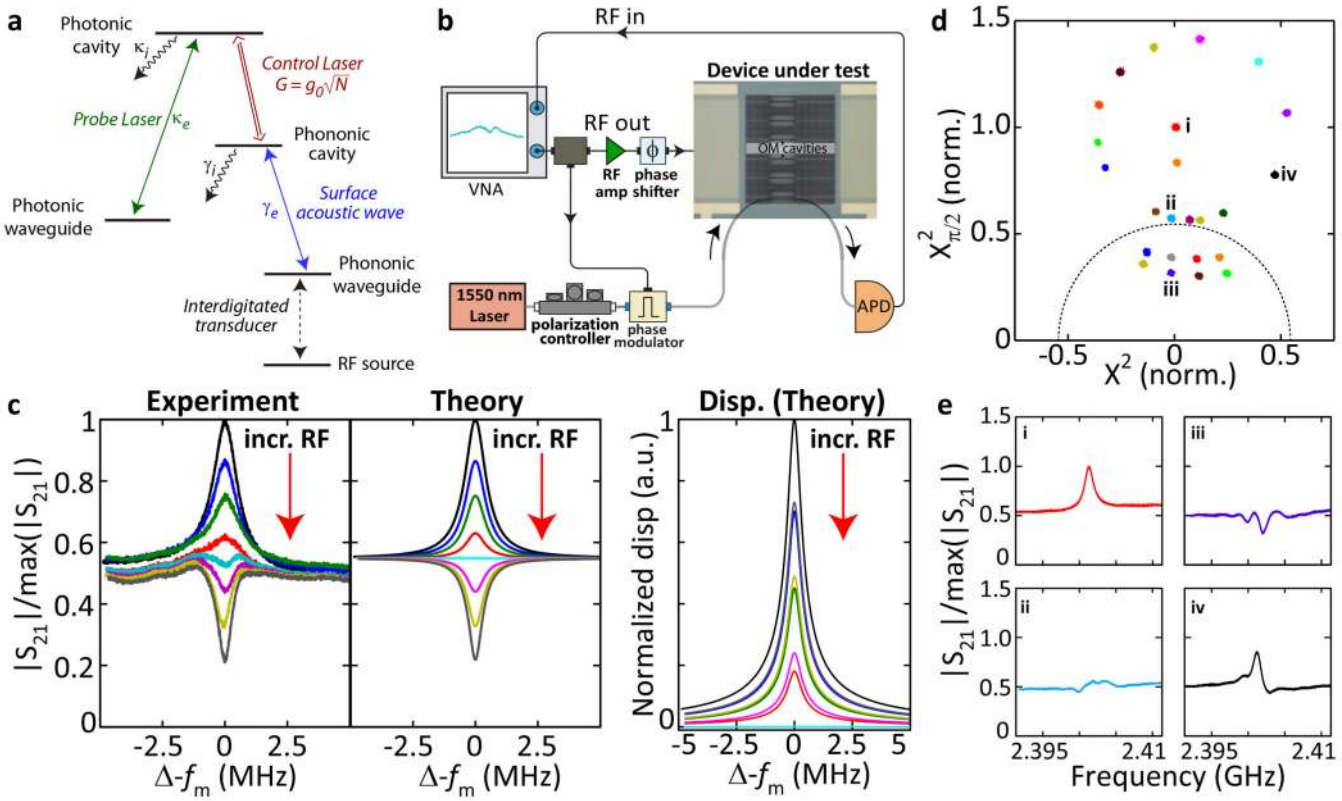

FIG. 4. Acoustic wave interference

(a) Level diagram indicating the phononic cavity population driven either optically or via RF-generated propagating acoustic waves. (b) Experimental setup. The VNA output is split and one part is sent to an electro-optic phase modulator for optically driving the phononic cavity. The other part is phase shifted, amplified, and sent to the IDT for an RF-generated acoustic wave drive. (c) Transmitted probe sideband spectrum as a function of RF power showing optomechanically-driven motion (RF = 0) (black), acoustic wave interference (cyan), and RF-dominated motion (dark gray) regimes (Experimental data on left, theory in center, and simulated cavity displacement on the right). (d) Coherent motion in phase space (bandwidth = 200 Hz). The black dashed semicircle is the off-resonance background. The four numbered points, with frequency response curves shown in (e), correspond to (i) optomechanically-driven motion, (ii) acoustic wave interference, (iii) RF-dominated motion, and (iv) Fano lineshape behaviour.